ELSEVIER

Contents lists available at ScienceDirect

Materials Today Communications

journal homepage: www.elsevier.com/locate/mtcomm



Thermophysical properties of additively manufactured (AM) GRCop-42 and GRCop-84

Yehong Chen ^a, Congyuan Zeng ^b, Huan Ding ^a, Selami Emanet ^a, Paul R. Gradl ^c, David L. Ellis ^d, Shengmin Guo ^a, ^{*}

- ^a Dept. Mechanical and Industrial Engineering, Louisiana State University, Baton Rouge, LA 70803, USA
- ^b Dept. Mechanical Engineering, Southern University and A&M College, Baton Rouge, LA 70807, USA
- NASA Marshall Space Flight Center, Huntsville, AL 35812, USA
- ^d NASA Glenn Research Center, Cleveland, OH 44135, USA

ARTICLE INFO

Keywords: GRCop Thermal conductivity Additive manufacturing Thermal diffusivity Thermal expansion

ABSTRACT

Additive manufacturing (AM) has enabled new opportunities of high-performance alloys for use in complex components across the aerospace, industrial, automotive, and energy industries. These industries have growing interest in copper alloys and AM for high-performance heat exchangers such as rocket engine combustion chambers. GRCop copper alloys, such as GRCop-84 (Cu-8Cr-4 Nb at%) and GRCop-42 (Cu-4Cr-2 Nb at%), have high thermal conductivity and high mechanical properties at elevated operating temperatures. In this paper, thermophysical properties for GRCop-84 and GRCop-42 produced using laser powder bed fusion (L-PBF) are examined. While L-PBF parameters and resulting microstructures can be achieved in a laboratory environment, those parameters do not always translate well into a production environment, and the variations across multiple machines and powder chemistries must be understood. The repeatability and reproducibility of samples across the commercial supply chain is critical for designers to ensure parts meet operational requirements. Thermophysical properties, such as thermal conductivity and thermal expansion are key design attributes. Thermal conductivities for eight GRCop-42 blocks and two GRCop-84 blocks were measured from room temperature up to 700 °C. Thermal expansion was also measured from 20 °C to 1000 °C. These GRCop alloy parts were made with gas atomized powders from different vendors and with different L-PBF systems and parameters. Equations for the thermal conductivity and expansion are given. The variation of thermal conductivities for L-PBF GRCop parts is estimated to be less than +/-4%. Based on phase analysis, compositional analysis, and thermal conductivity measurements, the small variations in thermal conductivities for the L-PBF GRCop parts are elucidated. The thermophysical property variations can be used to establish process capabilities and design guidelines for ongoing commercial use and further research.

1. Introduction

Metal additive manufacturing alloys are commonly used in various applications for medical, industrial, automotive, energy, and aerospace. Copper and its alloys are indispensable in many industries because of their high conductivity and corrosion resistance that make them useful for heat exchangers and other high thermal and electrical conductivity applications [1–6]. Multiple alloying elements, such as Cr, Zr, Al, Fe, Ti, and Nb, are commonly used to produce different copper alloys. For example, the Cu-Cr alloy has excellent mechanical performance [7–9]. With the addition of Nb, Zr, or Ag, the Cu-Cr alloys developed into a

ternary system (Cu-Cr-X) [10–12]. Compared to Cu-Cr-Ag and Cu-Cr-Zr ternary systems, Cu-Cr-Nb ternary alloy system exhibits significant advantages, such as high strength and excellent conductivity [13–16]. Furthermore, this ternary alloy system has high oxidation resistance [17, 18].

Among the Cu-Cr-Nb ternary alloys, the most prominent ones are GRCop-84 (Cu-8Cr-4 Nb at%) and GRCop-42 (Cu-4Cr-2 Nb at%). They were developed by NASA for regeneratively cooled rocket engine combustion chamber liners that require high-strength and high conductivity at elevated temperatures [19-21]. These GRCop alloys mainly depend on the Cr₂Nb Laves phases with the Cr and Nb atomic ratio of 2:1. For

E-mail address: sguo2@lsu.edu (S. Guo).

^{*} Corresponding author.

both GRCop-84 and GRCop-42, Cr and Nb are mostly kept in the $\rm Cr_2Nb$ Laves phases, and therefore, the matrix of the alloy is nearly pure copper and thus has an outstanding electrical and thermal conductivity [19,20]. GRCop-84 shows exceptional microstructural stability, creep resistance, good thermal conductivity, good low cycle fatigue life, and high tensile strength that are optimized for 500–800 °C. GRCop-84 also has a lower thermal expansion than Cu and dilute Cu-based alloys from room temperature up to 1000 °C [22]. Due to those characteristics, GRCop-84 exhibits good potential for high heat flux applications such as rocket combustion chambers, permanent metal casting mold, fusion reactors, welding electrodes, and high temperature heat exchangers [23,24].

GRCop-42 was created by decreasing the Cr_2Nb volume fraction to trade mechanical properties for improved thermal conductivity. The thermal conductivity of GRCop-42 is about 15% higher than GRCop-84. NASA widely adopted GRCop alloys for high heat flux applications [25] due to the capability of repeated use under high strain conditions with elevated wall temperatures. For example, GRCop-42 has been selected and is being flown on launch vehicles as the material for building additively manufactured channel-cooled combustion chambers for rocket engines [26,27].

Most materials expand upon heating. This thermal expansion can cause three issues for rocket engine liners. The first issue is the thermally induced stresses. The liner is typically constrained by a high-strength jacket that remains relatively cool. The liner cannot expand freely and the thermal expansion results in thermally induced stresses. For a liner application, the stresses can often exceed the yield strength of GRCop-42 and GRCop-84. The second issue is the permanent deformation of the material from these thermal stresses that can permanently change the shape of the liner. This can include the so-called "doghouse" effect [28] that can contribute to failure in the hot wall within a cooling channel. The third issue is low cycle fatigue (LCF), where a combustion chamber liner is repeatedly cycled for qualification or operation. The liner will be subjected to repeated strains locally from thermal expansion that can exceed 1%. This is one of the major contributors to liner failure [29].

The thermal conductivity and thermal expansion of GRCop alloys are controlled largely by the dissolved trace elements in the copper matrix and the amount and type of secondary phases present, respectively. The presence of Cr and Cr₂Nb precipitates reduces the thermal expansion of GRCop alloys relative to pure Cu [30], because these phases have lower thermal expansion than Cu [31]. The primary elements of concern for lowering the thermal conductivity are O from the environment, Fe from the Cr feedstock, and Al and Si from ceramic refractories used in melting the alloys [32]. Any excess Cr that is not precipitated will affect the thermal conductivity and thermal expansion.

To achieve the desired microstructure, thermophysical properties, and mechanical properties, GRCop alloys require high cooling rates during solidification. This is due to the Cr₂Nb quickly forming when the temperature drops just below the alloy liquidus temperature while copper is still in the molten state [33]. High cooling rates limit the size of Cr₂Nb phase and ensure a uniform distribution of the Cr₂Nb phase precipitates in the copper matrix. Conventionally, GRCop powders are manufactured by the gas atomization technique, which has a cooling rate of 10⁴ K/s[34]. More traditional manufacturing techniques, such as extrusion and hot isostatic pressing (HIPing), were used to consolidate GRCop powders. Subsequently, the consolidated material could be processed conventionally using methods such as rolling, forging, and tube drawing [35]. In comparison to GRCop-84, GRCop-42 can mitigate some of the high temperature requirements during the powder atomization process due to the lower liquidus temperature (1460 $^{\circ}\text{C}$ vs 1580 °C) resulting from the reduced content of Cr and Nb [26].

Metal additive manufacturing (AM) is a process that makes metallic parts layer by layer and has various build methods, including powder bed fusion, directed energy deposition, cold spray, additive friction stir deposition, and binder jetting [36]. In this paper, the GRCop samples are manufactured by laser powder bed fusion (L-PBF) AM. During the L-PBF process, thin layers of powder are spread on a build plate and scanned by

a high energy laser beam to melt localized areas. The laser fuses the powders and generates the specific geometry. After one layer is completed, another layer of powders is spread, and the same procedure repeated until the part is finished. Due to the small molten track size and rapid laser scanning, L-PBF process has a high cooling rate of 10^4 K/s to 10^6 K/s [37]. In the L-PBF AM process, the layer thickness of GRCop-42 is generally increased compared to GRCop-84, thus increasing the production rate [26].

While L-PBF processing can be demonstrated under controlled laboratory conditions, the process and inputs may experience variations when translated into a full production environment. The differences can be compounded when there are multiple producers using their own proprietary methods that may or may not be similar.

In this study, eight unique GRCop-42 samples and two unique GRCop-84 samples were built using different lots of gas atomized powders. The samples were produced using eight different vendors with their differing proprietary operating procedures including the use of mixed virgin and recycled powder. The use of recycled powder and multiple vendors is a realistic programmatic consideration to control production costs. As the GRCop alloys moved from laboratory into production environments, it was critical to understand these process capabilities and capture the resulting differences in microstructure, geometry, and properties. Samples were built by several vendors using various L-PBF machine platforms in the form of a feature build plate, which test specimens were excised from. The objective of this study was to analyze and compare the thermophysical properties, specifically thermal conductivity and thermal expansion, of samples produced by various vendors using different L-PBF platforms and powder batches. The aim was to assess the potential variability in thermophysical properties within the commercial vendor supply chain and establish process capabilities and design guidelines accordingly [38]. The intrinsic factors that influence the thermophysical properties of the GRCop alloys were also examined.

2. Materials and methods

2.1. Sample production

In this study, GRCop-42 and GRCop-84 copper-alloy feature build plates were produced by eight different vendors utilizing the Laser Powder Bed Fusion (L-PBF) process. Each vendor employed their specific L-PBF machines and slightly different parameters, often considered proprietary, to manufacture the plates. Standard L-PBF scan strategies were varied across platforms and recoater materials were used based on the vendor preferences [39]. The powder feedstock followed the GRCop-42 specification chemistry and powder size distribution (PSD) provided by Gradl et al. [40]. The powder feedstock included a mix of virgin powder and reuse per standard procedures for each of the suppliers. The reused powder was sieved to meet the $10-45 \mu m$ PSD with particles smaller than 10 µm limited to less than 5% cumulative volume (per ASTM B214) and particles greater than + 325 mesh limited to less than 1% weight (per ASTM B822). A mix of virgin and reuse powder is typical for production of parts to allow for the process to be economical. While the chemical composition was provided in powder certifications, the as-built chemistries are critical to understand the thermophysical properties and was measured as described in Section 3.1.

The L-PBF feature build plates were identical to those built under a prior study to assess geometric process capability of the commercial supply chain [38].

2.2. Chemical analysis

Chemical analysis of the metallic elements was conducted using inductively coupled plasma – atomic emission spectroscopy (ICP-AES) per CAP-017S and inert gas fusion (IGF) per ASTM E1019–18 using Perkin Elmer Optima 8300 and 7300. In addition to the major elements,

trace elements such as Fe that can reduce thermal conductivity were examined. A LECO Model ONH 836 is used to determine the amount of oxygen and nitrogen in the samples.

2.3. The apparatus and theory for thermal diffusivity/conductivity measurements

A Netzsch LFA 467 HT apparatus was used for thermal diffusivity/conductivity measurements. The schematic diagram of LFA test cell is shown in Fig. 1(a). It is designed as a vertical system with the energy (light) entering the cell from the bottom window. The sample is positioned in the center, and the infrared (IR) detector is above the top window. A xenon lamp works as a flash source. Software controls this flash with a pulse range of 20–1200 μs . After the flash of the xenon lamp irradiates the lower face of the sample, the temperature rise of the opposite side is measured as a function of time using the IR detector. Thermal diffusivity of the sample was determined from the temperature trace using the equation.

$$a = 0.1388 \times l^2 / t_{1/2} \tag{1}$$

where.

a is the thermal diffusivity in cm²/s.

l is the thickness of the test piece in cm.

 $t_{1/2}$ is the time (in second) at 50% of the temperature increase, measured on the top surface of the test piece.

The specific heat (*Cp*) of samples was determined by the Netzsch LFA 467 HT apparatus via a comparison measurement with a reference sample [41]. Thermal conductivity was calculated using the following equation:

$$K(T) = C_p(T) \times a(T) \times \rho(T) \tag{1}$$

where.

K(T) is the temperature-dependent thermal conductivity of the testing sample.

 $C_p(T)$ is the temperature-dependent specific heat.

a(T) is the temperature-dependent thermal diffusivity.

 $\rho(T)$ is the temperature-dependent density of the testing samples.

2.4. Thermal Diffusivity/Conductivity Measurements: Sample Preparation and Testing

The sample details are described in Table 1. Three disk-shaped samples were excised from each of the feature build plates following HIP, with a diameter of 12.56 mm and a thickness of \sim 2.5 mm. Prior to the thermal diffusivity/conductivity testing, the disks were ground with

400 grit SiC sandpaper to remove the surface contaminant layer. Densities of the samples at room temperature were measured based on Archimedes principle. The elevated temperature densities were determined using thermal expansion data based on a previous study [42]. For each run, three samples from a GRCop build and a copper reference sample (99.999% purity) were sprayed with graphite. This was to ensure identical energy absorption during the thermal diffusivity/conductivity test process described in Section 2.3. Detailed thermal conductivity test procedures can be found in prior studies [43].

Following an initial run of each sample, the samples and the reference sample were rinsed with ethanol in an ultrasonic tank to remove the graphite layer. After thorough drying, the samples together with the reference sample were once again spray coated with graphite before the repeated testing of thermal diffusivity/conductivity.

Eight GRCop-42 and two GRCop-84 L-PBF sample groups were examined. For each group, three samples from each alloy block were measured at 25 °C, 100 °C, 200 °C, 300 °C, 400 °C, 500 °C, 600 °C, and 700 °C. At each measurement temperature, three measurements for each sample were taken (nine measurements total). After the first cycle of tests was finished, a second test cycle was repeated from 25 °C to 700 °C.

2.5. Phase Identification

To simplify the analysis of the phases and determine the total amount present, the phases were extracted from the copper matrix. The concentrated precipitates also allowed for a higher probability of finding small amounts of a phase that would be masked by the Cu matrix in x-ray diffraction (XRD).

Approximately 1 g of sample was placed in concentrated nitric acid. The acid dissolved the copper matrix but did not attack any of the phases of interest. The samples were allowed to react until all the copper was dissolved. The remaining material was filtered through a 0.45 μm filter paper. Using the weights of the original sample and filtrate, the total amount of precipitates in the samples were calculated.

Some of the filtrate was removed from the filter paper with a razor blade and transferred to a low background XRD holder. Isopropyl alcohol was used to disperse the precipitates in a thin, uniform layer. Data were gathered on a D8 Advance diffractometer using Cu Ka radiation. Four-hour scans were performed to help find any trace phases.

Quantitative phase analysis (QPA) was performed using whole pattern fitting (WPF, aka, Rietveld refinement) as implemented in the JADE analysis program. In addition, the materials were examined before and after extraction using a TESCAN MAIA-3 scanning electron microscope (SEM). An energy dispersive spectrometer (EDS) unit on the SEM was used to determine the chemistry of the precipitates and help identify

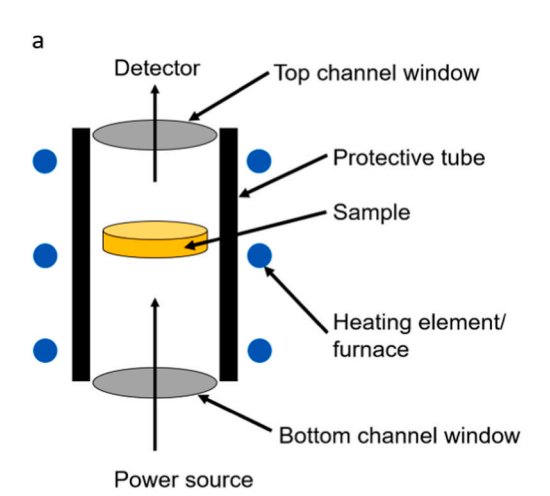




Fig. 1. (a) Schematic diagram of LFA testing cell. (b) LFA 467 HT has four testing cells, the Top Window of the top-right cell is removed for sample installation.

Table 1GRCop L-PBF blocks tested for thermal conductivities.

Identifier	Alloy	Company	Machine	Layer Height (um)	Recoater Type	Energy Density (J/mm^3)	Scan Strategy[39]
GRCop-42-1	GRCop-42	Α	EOS M280	40	Rubber	75.0	Continuous
GRCop-42-2	GRCop-42	В	EOS M290	45	Steel	90.3	Stripes
GRCop-42-3	GRCop-42	В	EOS M400-1	60	Steel	83.3	Stripes
GRCop-42-4	GRCop-42	C	EOS M400-1	40	Rubber	75.0	Continuous
GRCop-42-5	GRCop-42	Α	EOS M280	40	Steel	75.0	Continuous
GRCop-42-6	GRCop-42	D	EOS M290	40	Carbon Fiber Brush	-	-
GRCop-42-7	GRCop-42	E	EOS M400-4	60	Steel	83.3	Stripes
GRCop-42-8	GRCop-42	F	EOS M290	45	Carbide	90.3	-
GRCop-84-1	GRCop-84	G	Concept M2	30	Rubber	100.0	Checkered
GRCop-84-2	GRCop-84	Н	EOS M290	40	Steel	107.1	Stripes

The parameters not provided were considered proprietary and not publishable.

them.

2.6. Thermal expansion

Ten samples nominally 20–22 mm long were cut from portions of the feature build plates. The cross-sections were roughly rectangular, but no effort was made to have a consistent, uniform cross-section for the samples as it is not required for thermal expansion measurements. The ends were parallel and were confirmed to have the same area.

The samples were cycled three times in a Netsch model DIL402C dilatometer. The samples were heated in argon to prevent oxidation. A thermocouple placed near the sample recorded the temperature while a linear variable differential transformer (LVDT) measured the displacement of the sample as it heated. The contribution of the furnace tube, push rod, and other parts of the heated section expanding was mathematically removed using a calibration run with alumina to calculate the net thermal expansion of the instrument. The difference was the change in length for the sample (ΔL). The thermal expansion or thermal strain at a temperature T (ϵ_T) was calculated as

$$\varepsilon_T = \Delta L_T / L_0 \tag{3}$$

where

 L_0 is the initial length of the sample.

 ΔL_T is the measured change in length at temperature T; and.

 ε_T is the thermal expansion at temperature T.

The coefficient of thermal expansion (CTE) is often used to calculate the thermal expansion of a part. There are two types of thermal expansion coefficients. The first and more commonly used one is the average thermal expansion. The average CTE (CT $_{\rm Average}$) at a given temperature is defined as

$$CTE_{Average_T} = \varepsilon_T / (T - T_{Ref}) \tag{1}$$

where.

T is the temperature of interest; and.

 T_{Ref} is the reference temperature where the thermal expansion is defined as 0. For this study, T_{Ref} was defined as 293 K or 20 $^{\circ}$ C.

The instantaneous CTE ($CTE_{Instant}$) is the derivative of the thermal

expansion curve at a given temperature and is independent of the reference temperature. The value was approximated by the slope of the curve over five data points centered at the temperature of interest. A least squares residual fit of a line was made to the points, and the slope calculated by Microsoft Excel.

3. Results

3.1. Chemistry

The results of the chemical analysis are show in Table 2. The main source of chemical difference is the normal lot-to-lot variability in powder composition. This is recognized in the specifications for most alloys that include a range rather than a single value for each element. In the case of GRCop, the main source is likely problems encountered with dissolving the Nb into molten Cu, which results in low Nb. The Cr also was at the low end of the specified range, likely for the same reason, which is why the ratios are generally acceptable. Other elements are generally associated with trace contaminant in the melt stock, e.g., Ag in Cu and Fe in Cr. In addition to the major elements of Cu, Cr, and Nb, some trace elements like Fe, Al and Si were also detected. The oxygen content is higher in the GRCop-84 samples since older, off-the-shelf GRCop-84 powders were used that might have more oxidation from its time in storage [44]. There are various sources for the oxygen in the powder feedstock as copper is prone to oxidation, even at room temperature. The objective of this study was to capture the variations of the powder across the supply chain, which includes the oxygen content. The sources of the oxygen pickup include: 1) Incorporation of refractory ceramic particles (alumina, niobia) into the atomization of the powder, 2) Recycling of the powder and exposure to air outside the build chamber during sieving, 3) Powder handling and surface oxidation, and 4) Atmosphere control during printing.

3.2. Thermal Conductivity of GRCop Alloys

As shown in Fig. 2, the thermal conductivity of the GRCop alloys normally decreases with increasing test temperature. Based on the average of the measured values for the eight GRCop-42 samples, the

 Table 2

 Weight percentage of elements in the tested GRCop alloys.

Element	GRCop-42-1	GRCop-42-2	GRCop-42-3	GRCop-42-4	GRCop-42-5	GRCop-42-6	GRCop-42-7	GRCop-42-8	GRCop-84-1	GRCop-84-2
Ag	0.01	< 0.01	< 0.01	< 0.01	< 0.01	< 0.01	< 0.01	< 0.01	< 0.01	< 0.01
Al	0.06	0.06	0.06	0.06	0.06	0.07	0.04	0.06	0.01	0.03
Co	0.01	< 0.01	< 0.01	< 0.01	< 0.01	< 0.01	< 0.01	< 0.01	< 0.01	< 0.01
Cr	3.25	3.30	3.29	3.37	3.26	3.28	3.28	3.38	6.61	6.59
Fe	0.01	< 0.01	< 0.01	< 0.01	0.01	< 0.01	< 0.01	< 0.01	< 0.01	< 0.01
Nb	2.65	2.82	2.77	2.81	2.65	2.92	2.73	2.92	5.68	5.47
Ni	0.03	< 0.01	< 0.01	0.01	0.02	< 0.01	0.01	< 0.01	< 0.01	< 0.01
O	0.08	0.05	0.04	0.06	0.1	0.05	0.08	0.05	0.13	0.12
P	< 0.005	< 0.005	< 0.005	< 0.005	< 0.005	< 0.005	< 0.005	< 0.005	< 0.005	0.011
Si	0.02	0.01	< 0.01	0.03	0.04	0.01	< 0.01	0.02	< 0.01	< 0.01

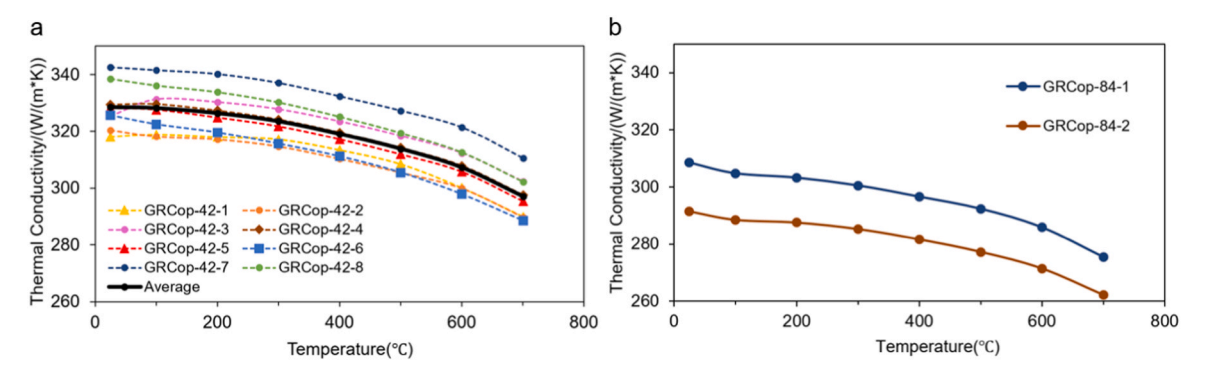


Fig. 2. (a) Thermal conductivity of different GRCop-42 L-PBF samples. (b) Thermal conductivity of GRCop-84 L-PBF samples.

conductivity value can be curve-fitted to the equation over the temperature range of 25 $^{\circ}\text{C}$ to 700 $^{\circ}\text{C}$

$$k(T) = -39.86T^3 + 4.17T^2 + 0.97x + 329.14$$
 (3)

where T is temperature in K/1000.

It was observed that the range of the thermal conductivities of all GRCop-42 alloys, except sample GRCop-42–7, fall within the unit's specified uncertainty of 3% in the equipment manual. As for GRCop-42–7, its thermal conductivity values are about 8% higher than the sample GRCop-42–1, the lowest thermal conductivity sample. For GRCop-84, there were only two samples. As presented in Fig. 2(b), there is a difference up to 7% observed between GRCop-84–1 and GRCop-84–2.

The directly measured thermal diffusivities for all GRCop samples are presented in Fig. 3. According to the equation K(T)=Cp (T)× $\alpha(T)\times \rho$ (T) as we mentioned, the α is proportional to K at a specific temperature. Therefore, thermal diffusivities have the same variation trend as thermal conductivities.

3.3. Problem Encountered During Thermal Conductivity Testing: Specific Heat Measurement

During the data analysis, numerous specific heat measurement datasets were identified to be inaccurate due to contamination of the bottom windows in the test cells. As stated in 2.3, the signal obtained from the sample is compared with the signal generated on the reference for specific heat measurements. The assumption is that the same amount of energy was absorbed by both the samples and the reference. This assumption is valid if the optical transparencies for all four of the testing cells are the same. The top windows of the test cells are easily accessible, and they are cleaned regularly to maintain the identical optical transparency. The bottom windows of the test cells are not readily accessible since that involves the dismantlement of the machine. Typically, window contamination should not occur. Unfortunately, the LFA 467 HT

system was also used to measure thermal conductivities of bio-derived particles during prior research. Some bio particles, mainly soot, contaminated the bottom windows of the test cells.

As shown in Fig. 3, a clean window allows much more energy to pass through into the test cell. In contrast, for a contaminated window, a reduced amount of energy would pass through into the test cell. This would lead to a reduced sample temperature rise and a wrongly interpreted high specific heat value. For example, one GRCop specimen and a Cu reference sample were placed into the contaminated equipment. The reported specific heat of this specimen in the contaminated cell was around 0.520 J/(g K), which is much larger than the theoretical value of 0.383 J/(g K) at 25 °C. To diagnose the issue, the specimen and reference sample positions were swapped, and the test repeated. In the second run, the specimen exhibited a specific heat of 0.303 J/(g K) at 25 °C, which confirms the diagnostics that the test cell windows were contaminated and would influence the specific heat result.

As a comparison to the experimental results, the specific heat values of Cu, Cr, and Nb from NIST [45] can be used to estimate the specific heat values for GRCop-42 and GRCop-84. NIST provides specific heat of the elements at different temperatures. The specific heat can be calculated using the following equation:

$$Cp(alloy) = m_1 Cp(Cu) + m_2 Cp(Cr) + m_3 Cp(Nb)$$
(6)

where.

Cp(Cu), Cp(Cr), and Cp(Nb) are the specific heat capacity at the corresponding temperatures; and m_1 , m_2 , and m_3 are the mass fraction of the related metal elements.

The specific heats of Cu, Cr, and Nb and the calculated specific heats of GRCop-42 and GRCop-84 are shown in Table 3. Curve fitting can be used to describe the specific heat of GRCop-42 and GRCop-84 over the temperature range of 25 °C to 700 °C. The resulting equations were

$$GRCop - 42: C_p = 0.153T^3 - 0.33T^2 + 0.312T + 0.316$$
(7)

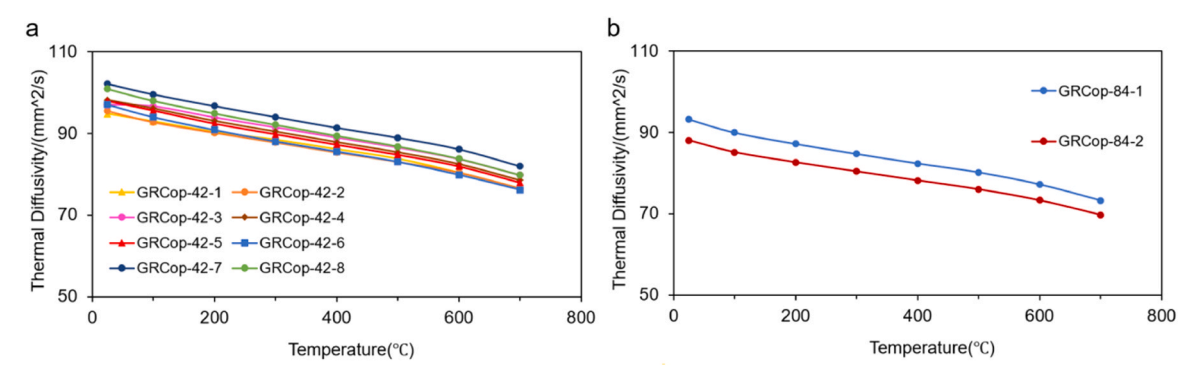


Fig. 3. (a) Thermal diffusivity of different GRCop-42 L-PBF samples. (b) Thermal diffusivity of GRCop-84 L-PBF samples.

Table 3Calculated specific heat of Cu, Cr, Nb, GRCop-42, and GRCop-84 at different temperatures.

Р					
Temperature (°C)	Cu (J/ (g K))	Cr (J/ (g K))	Nb (J/ (g K))	GRCop-42 (J/ (g K))	GRCop-84 (J/ (g K))
25	0.385	0.451	0.266	0.384	0.383
100	0.395	0.477	0.271	0.394	0.393
200	0.407	0.506	0.277	0.406	0.405
300	0.416	0.528	0.282	0.416	0.415
400	0.424	0.542	0.287	0.424	0.423
500	0.431	0.558	0.292	0.431	0.431
600	0.438	0.580	0.296	0.439	0.439
700	0.448	0.607	0.301	0.449	0.449

$$GRCop - 84: C_p = 0.165T^3 - 0.353T^2 + 0.329T + 0.311$$
(8)

where x is the temperature in K/1000.

A plot displaying GRCop specific heats is shown in Fig. 4.

3.4. Phase Identification

Representative SEM images from Sample GRCop-42–4 are shown in Fig. 5. The larger spherical particles were identified as NbO using EDS and XRD. The smaller particles were identified as primarily Cr₂Nb. Cr precipitates do not image well in secondary electron (SE) mode due to low atomic number (Z) contrast with Cu. Fig. 5(a) shows that there is a uniform distribution of Cr₂Nb throughout the Cu matrix. There appears to be variability in the size of the Cr₂Nb particles, and this is confirmed in the extracted particles recovered from the filtrate (Fig. 5b). Full particle size analysis was not conducted, but most precipitates are $<1~\mu m$ in diameter.

The XRD scans were combined into a single plot that is presented in Fig. 6.

It was observed that Samples GRCop-42–4 and GRCop-42–1 had a very poor fit to their NbO peaks that resulted in an overestimation of the amount present (Fig. 7). The cause for the peak fitting issue could not be identified, and repeats of each sample were tested. The results again showed an unusually broad NbO peak that was not present in Samples GRCop-42–2 and GRCop-42–7. The decision was made to note that NbO had been found but not report the absolute value. The remaining phases were normalized so that they summed to 100%. The error was deemed to be acceptable as the amount of NbO was clearly small.

The total amount of precipitate and the phases present for each sample are listed in Table 4. As expected, there was a significant difference in the total amount of precipitates between the GRCop-42 and GRCop-84 samples. Also as expected based upon the chemistries, those with high Cr:Nb ratios had significant amounts of elemental Cr.

Small amounts of CuO were observed in some samples. Most likely this is leftover matrix that had oxidized while the filtrate was exposed to air. Significant amounts of NbO were found in three samples with three

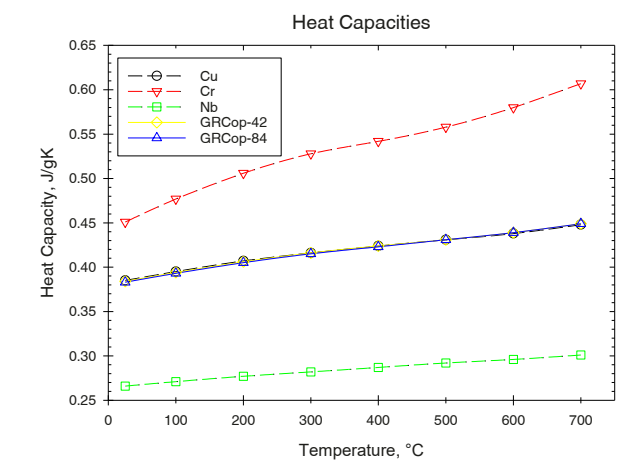


Fig. 5. Calculated Specific heat for Cu, Cr, Nb, GRCop-42, and GRCop-84.

other samples having detectable amounts present. The NbO particles were observed in the SEM to have an alumina core from detection. The NbO appears to have been thick enough to shield the alumina in XRD. The NbO was believed to come from reaction between the Nb in the molten alloy and alumina crucible used for the melting process [46].

GRCop alloys are designed to have a small excess of Cr to drive down the activity of the Nb in Cr₂Nb and prevent hydrogen embrittlement [47]. The amount of elemental Cr is typically "1 wt% in extruded GRCop-84 and should be similar in GRCop-42. Considering the fraction of the total amount of precipitates that are elemental Cr, the total weight fraction of Cr ranged from 0.34 to 1.48 wt%. This is generally consistent with past work although the ratio of Cr to Cr₂Nb for Samples GRCop-42–5 and GRCop-84–6 were much higher than the average 0.08 for the other samples. Samples GRCop-42–5 and GRCop-42–6 had roughly a quarter of their precipitates being Cr.

While not ideal, the chemistries of the samples and the phases present are generally representative of what should be expected in AM GRCop alloys and consistent with past extruded GRCop alloy samples tested for thermal conductivity and thermal expansion.

3.5. Thermal Expansion

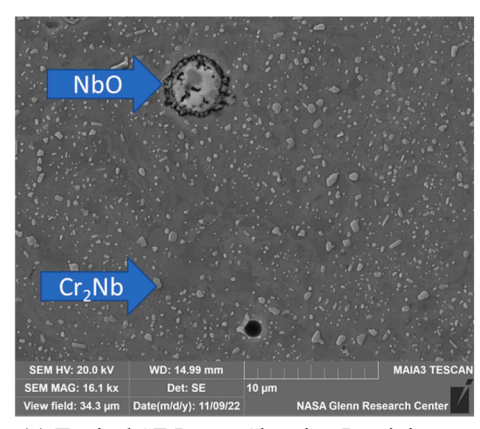
The average thermal expansion curves using the data from Cycles 2 and 3 are shown in Fig. 8. A 50 $^{\circ}$ C interval was chosen for reporting the data. The average and instantaneous CTEs are presented in in Fig. 9 and Fig. 10, respectively.

The individual plots for the average and instantaneous thermal expansion cycles of each of the samples are provided in Appendices C through H for GRCop-42 and for GRCop-84. There are many details provided in the individual graphs that are not captured in the summary plots. The first cycle in each case was slightly different from the second

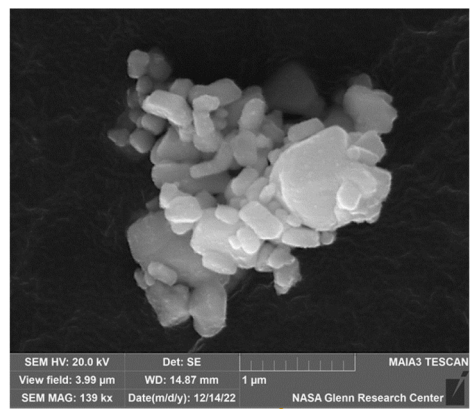




Fig. 4. (left) Testing cell window with minor contamination. (right) Testing cell window with overloaded contaminations.







(b) Typical Filtrate

Fig. 6. SEM Images of Particles.

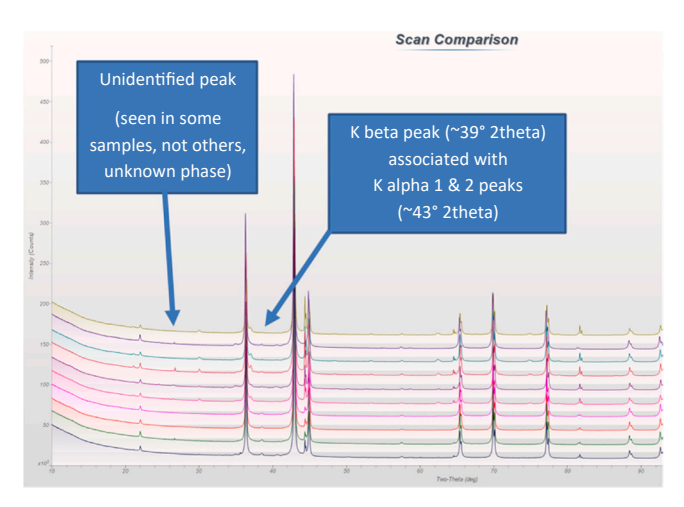


Fig. 7. X-ray Diffraction (XRD) Scans of the Extracted Precipitates.

Table 4 Amount and Types of Phases Present.

Sample	Alloy	Total (wt%)	Cr ₂ Nb	Cr	NbO	Cu ₂ O
GRCop-42-1	GRCop-42	6.83	83.9	7.3	-	5.5
GRCop-42-2	GRCop-42	7.12	90.7	8.7	0.6	
GRCop-42-3	GRCop-42	7.26	94.4	5.6		
GRCop-42-4	GRCop-42	6.05	93.5	5.6		1.9
GRCop-42-5	GRCop-42	6.27	74.7	23.6		1.7
GRCop-42-6	GRCop-42	4.92	74.7	23.6		1.7
GRCop-42-7	GRCop-42	7.55	86.2	7.8	6.0	
GRCop-42-8	GRCop-42	7.17	94.0	6.0		
	Average	6.64	86.5	11.0		
Nominal Cr ₂ Nb		6.1				
GRCop-84-1	GRCop-84	12.69	82.7	10.0	7.3	
GRCop-84-2	GRCop-84	12.70	81.4	11.2	7.5	
	Average	12.70	82.1	10.6		
Nominal Cr ₂ Nb		12.3				

and third cycles. The results tended to be similar for all three cycles above 300 $^{\circ}$ C, but the data was still not consistent. The first cycle can include precipitation of Cr, physical shifting of the sample, and creep. It was decided to not use the first cycle in calculations of the thermal expansions and CTEs and instead average the values for Cycles 2 and 3.

Above 900 $^{\circ}$ C, the force applied by the push rod can result in creep. This is most obvious in the instantaneous CTE curves where there is a distinct, dramatic decrease in the CTE values. While a correct measurement, the values do not reflect the thermal expansion alone. For that reason, the data points were not used for calculating the average of all

samples for the average and instantaneous CTEs. These data points are shown in orange in the individual plot in the appendices.

Polynomial regression was conducted using SigmaStat 3.5 to determine the order for fitting each curve. The order selected was determined using either the Mean Square Residual (MSR) decreasing with higher orders or engineering judgement when MSR became essentially constant. Where one alloy showed decrease in MSR while the other did not, the order of the equation for the first alloy was used.

The confidence interval can be estimated by multiplying the standard error of estimate ($S_{Y,X}$) by the t-value for the desired probability (1- α) and number of observations (n) minus the order of the equation. The fitted equations with the approximate confidence intervals for each alloy are

Thermal Expansion:

$$\varepsilon_{T,GRCop-42} = -5.89 \times 10^{-4} + 1.51 \times 10^{-5} (T - 273) + 6.28$$
$$\times 10^{-9} (T - 273)^2 - 1.88 \times 10^{-12} (T - 273)^3 \pm 1.88$$
$$\times 10^{-4} \quad t(1 - \alpha/2, 324) \tag{9}$$

$$\varepsilon_{T,GRCop-84} = -6.92 \times 10^{-4} + 1.59 \times 10^{-5} (T - 273) + 1.63 \times 10^{-9} (T - 273)^2 + 1.58 \times 10^{-12} (T - 273)^3 \pm 1.14 \times 10^{-4} t (1 - \alpha/2, 78)$$
(10)

Instantaneous CTE:

$$CTE_{Instant,GRCop-42}(ppm/K) = -8.55 + 0498(T - 273) + 3.49$$

$$\times 10^{-3}(T - 273)^{2} + 1.24$$

$$\times 10^{-5}(T - 273)^{3} - 2.47$$

$$\times 10^{-8}(T - 273)^{4} + 2.77$$

$$\times 10^{-11}(T - 273)^{5} - 1.65$$

$$\times 10^{-14}(T - 273)^{6} + 4.03 \times 10^{-18}(T - 273)^{7}$$

$$\pm 0.580t(1 - \alpha/2, 304)$$
(11)

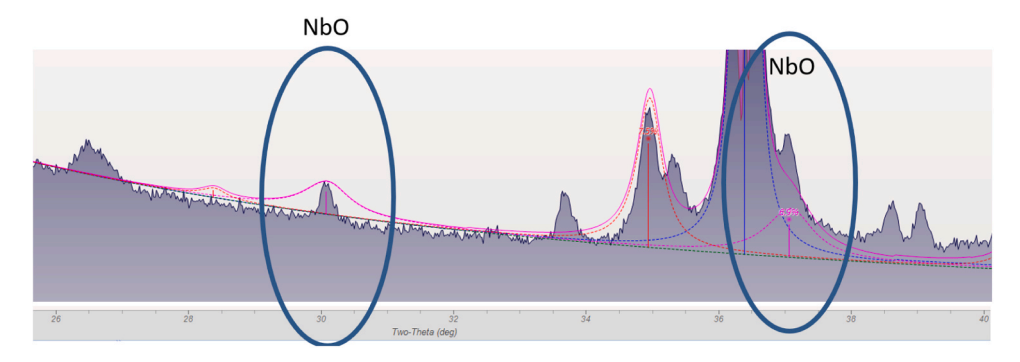


Fig. 8. Poor Fit of NbO Peaks for Sample GRCop-42-4.

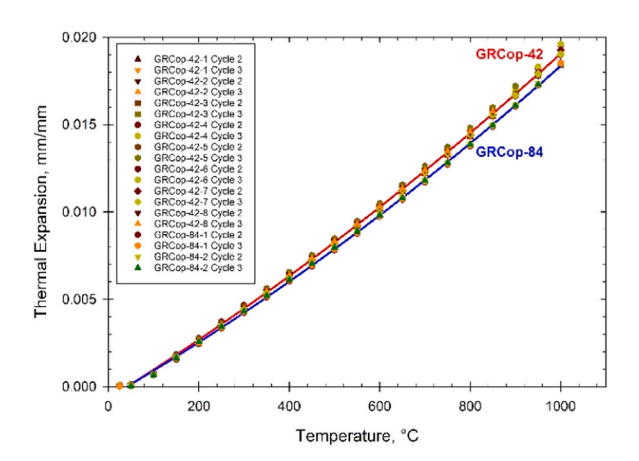
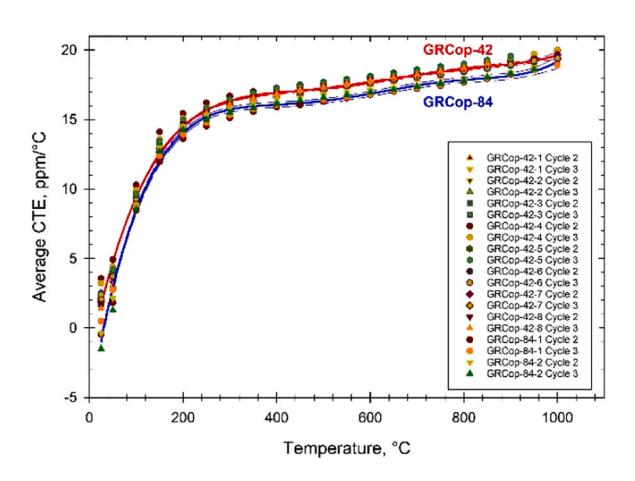


Fig. 9. Average Thermal Expansion of all samples.



 $\textbf{Fig. 10.} \ \ \text{Average CTE and Regression Lines of all samples}.$

$$CTE_{Instant,GRCop-84}(ppm/K) = -15.1 + 0.719T - 6.13$$

$$\times 10^{-3} (T - 273)^{2} + 2.74$$

$$\times 10^{-5} (T - 273)^{3} - 7.12$$

$$\times 10^{-8} (T - 273) + 1.12$$

$$\times 10^{-10} T (T - 273)^{5} - 1.04$$

$$\times 10^{-13} (T - 273)^{6} + 5.31$$

$$\times 10^{-17} (T - 273)^{7} - 1.14 \times 10^{-20} (T - 273)^{2}$$

$$\pm 0.426t (1 - \alpha/2, 72)$$
(12)

Average CTE:

$$CTE_{Average,GRCop-42}(ppm/^{\circ}C) = -2.04 + 0.160(T - 273) - 5.42$$

$$\times 10^{-4}(T - 273)^{2} + 9.00$$

$$\times 10^{-7}(T - 273)^{3} - 7.18$$

$$\times 10^{-10}(T - 273)^{4} + 2.21 \times 10^{-13}(T - 273)^{5}$$

$$\pm 0.411t(1 - \alpha/2, 318)$$
(13)

$$CTE_{Average,GRCop-84}(ppm/^{\circ}C) = -5.49 + 0.201(T - 273) - 7.34$$

$$\times 10^{-4}(T - 273)^{2} + 1.30$$

$$\times 10^{-6}(T - 273)^{3} - 1.09$$

$$\times 10^{-9}(T - 273)^{4} + 3.52 \times 10^{-13}(T - 273)^{5}$$

$$\pm 0.408t(1 - \alpha/2, 75)$$

The plots of the combined data and regressions are shown in Fig. 8 through Fig. 10. No confidence interval lines are shown in Fig. 8 because the confidence interval falls within the width of the regression line.

4. Discussion

4.1. Thermal Stability of GRCop Alloys

The phase structures as a function of temperature under equilibrium state for both the GRCop-42 and GRCop-84 alloys were simulated using Thermo-Calc software with the TCCU3 database. Mole ratios of 94:4:2 (GRCop-42) and 88:8:4 (GRCop-84) were applied for the calculation. For GRCop-42 alloy and GRCop-84 alloy, it was found that the solidus temperatures were around 1040 °C and 1080 °C, respectively. As the maximum thermal conductivity test temperature was 700 °C, no liquid phase should form in the GRCop alloy system during the thermal conductivity testing. Thus, the possibility of components dissolving in the liquid phase leading to the thermal diffusivity change could be excluded.

There are three phases existing in the diagram at room temperature,

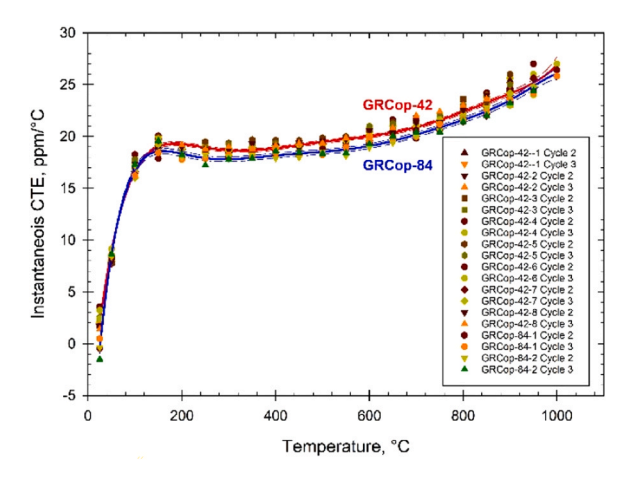


Fig. 11. Instantaneous CTE and Regression Lines of all samples.

Table 5Phase structures for the GRCop-42 and GRCop-84 alloys and the corresponding temperature ranges the phases exist under equilibrium states.

Phases with Thermo-Calc IDs	Phase	Stable temper	ature range (°C)
		GRCop-42	GRCop-84
FCC_L12 C15 LAVES	α-Cu Cr ₂ Nb	RT-1040 RT-1480	RT-1080 RT-1580
BCC_B2	Cr	RT-70	RT-75

namely Cr₂Nb phase (C15_LAVES), α -Cu phase (>99 wt% Cu, FCC_L12) and trace amounts of Cr phase (BCC_B2). As illustrated by Fig. 11, the temperature ranges within which the phases exist are listed in Table 5. For the GRCop-42 alloy, the Cr₂Nb phase predominantly maintains a consistent mole fraction of approximately 6% over the temperature range of 0–1040 °C. Above this threshold, the mole fraction begins to decrease gradually, eventually diminishing to zero at 1480 °C. Concurrently, at precisely 1040 °C, the α -Cu phase undergoes a phase transition to a liquid state, while the Cr₂Nb phase experiences a gradual transformation to the liquid state between 1040 and 1480 °C.

GRCop-84 exhibits the same phases as GRCop-42, and its phase diagram demonstrates a similar behavior to that of GRCop-42. As depicted in Fig. 11(b), during equilibrium cooling, the formation of the Cr₂Nb phase commences at a temperature of 1580 °C. In a manner akin to GRCop-42, the Cr₂Nb phase maintains a nearly consistent quantity from room temperature (RT) to 1080 °C. Furthermore, the quantity of the Cr₂Nb phase steadily decreases from 1080 °C to 1580 °C, ultimately vanishing. The findings derived from the phase structures corroborate the persistent thermal conductivity and thermal expansion results, which remained stable across multiple testing cycles from room temperature to 700 °C.

4.2. Possible Reason for the Variations in Thermal conductivities

With different powder sources and different L-PBF systems/parameters, the variations of GRCop thermal conductivities are up to about +/-4% of the mean value (Fig. 2), which is slightly higher than the equipment uncertainty associated with the thermal conductivity measurements (+/-3%). These small variations could be explained partially by the difference in contents of alloying elements.

For the tested GRCop-42 and GRCop-84 alloys, the mass percentages of compositional elements were tested using inductively coupled plasma atomic emission spectroscopy (ICP-AES) and inert gas fusion (IGF), and the test results are shown in Table 2. Apart from Cu, Cr, and Nb, the remaining elements listed in Table 2 are impurities. According to Table 2, the concentrations for Ag, Al, Co, Fe, Ni, O, P, and Si are low.

Table 6Solubility of elements in Cu.

Element	Composition wt% in Cu
Ag	0–8.8
Al	0-9.4
Co	0–7
Cr	0-0.73
Fe	0-4.1
Nb	0-0.15
Ni	Up to 100
O	0-0.008
P	0-1.7
Si	0–5

The binary phase diagrams for Ag-Cu, Al-Cu, Co-Cu, Fe-Cu, Ni-Cu, O-Cu, P-Cu, and Si-Cu were also analyzed to discover the range of solubility of different elements in copper over different temperature ranges, which is shown in Table 6. According to Table 6, nickel can completely dissolve in copper and up to 5% Si can dissolve in copper at high temperatures. The other elements have a high solubility in copper at elevated temperature that decreases to very low solubility when the temperature drops. L-PBF process is an extremely fast melting and solidification process, which could be far from equilibrium state shown in Fig. 11. To thermodynamically simulate the fast-cooling process, Scheil Solidification Mode was applied, through which the content of alloying elements in Cu matrix was estimated, and the calculation results are shown in Table 7.

According to prior research, in the case of a Cu-10Sn alloy, the presence of a dual-phase constituent (comprising both a Cu-rich phase and a Sn-rich phase) significantly reduces the number of solute atoms in the α -Cu phase (which is nearly pure Cu). This reduction has a marked effect on enhancing the alloy's thermal conductivity, largely due to the increased thermal conductivity (due to reduced Sn solution atoms) within the α -Cu phase itself. Thus, a Cu alloy that contains an α -Cu phase with a smaller quantity of solute atoms has a higher likelihood of exhibiting enhanced thermal conductivity [43]. Solution atoms affect thermal conductivity through two ways. As is widely accepted that thermal conductivity is mainly composed of two parts, namely electronic thermal conductivity governed by electrons, and lattice thermal conductivity conducted by crystal lattice. Solute atoms are strong scattering centers for electrons, in which directly increases electrical resistivity [48]. With the help of Wiedemann-Franz Law [49], over the thermophysical property test temperatures in this study, the increase of electrical resistivity indicates the increase of electronic thermal resistance, consequently reducing electronic thermal conductivity. Furthermore, the presence of solute atoms disrupts the regularity of the crystal lattice, impeding the efficient transfer of thermal energy by phonons and, in turn, lowering the lattice thermal conductivity of the alloy [50]. Phosphorous is a potent element for decreasing the thermal conductivity of Cu with Fe, Co, and Si being only slightly less deleterious [51]. Other elements such as Ag, Al, and Ni have much less effect on thermal conductivity [51]. Based on the discussion above, and by comparing thermal conductivity values of GRCop-84-1 and GRCop-84-2 alloy samples, it is very likely that the higher thermal conductivity of the former is due to the clearly reduced Phosphorous level.

The three low thermal conductivity samples for GRCop-42 alloys (Fig. 2(a)) are GRCop-42–1, GRCop-42–2, and GRCop-42–6. Coincidently, GRCop-42–1 has slightly higher Ni content, GRCop-42–2 possesses a high level of Cr content, while GRCop-42–6 has the highest Al content (Table 7). Specifically, based upon the effects of Cr on electrical conductivity [48], a linear decrease in thermal conductivity of 28% or about 110 W/(mK) for a 0.01 wt% Cr dissolved in the Cu matrix was expected [43]. However, for GRCop-42 alloy samples, only analyzing from the perspective of solution atom contents is not enough. One discrepancy is the sample GRCop-42–3, which has high levels of Al and Cr elements, but still with high thermal conductivity values over the test

Table 7 Contents of alloying elements in α -Cu phase under fast cooling state (Scheil solidification model).

Element in FCC_L12 (wt %)	GRCop- 42–1	GRCop- 42–2	GRCop- 42–3	GRCop- 42–4	GRCop- 42–5	GRCop- 42–6	GRCop- 42–7	GRCop- 42–8	GRCop- 84–1	GRCop- 84–2
Ag	0.0715	0.0639	0.0629	0.0713	0.0716	0.0657	0.0715	0.0654	0.0692	0.0753
Al	0.0000	0.0037	0.0148	0.0000	0.0000	0.0136	0.0000	0.0037	0.0000	0.0000
Co	0.0001	0.0001	0.0001	0.0001	0.0001	0.0001	0.0001	0.0001	0.0001	0.0001
Cr	0.5212	0.6024	0.6042	0.5134	0.5398	0.5978	0.5421	0.5809	0.5464	0.5121
Fe	0.0044	0.0037	0.0038	0.0035	0.0053	0.0036	0.0048	0.0038	0.0064	0.0057
Nb	0.0000	0.0001	0.0001	0.0000	0.0000	0.0001	0.0000	0.0001	0.0001	0.0000
Ni	0.0090	0.0028	0.0028	0.0025	0.0068	0.0027	0.0032	0.0028	0.0047	0.0039
O	0.0043	0.0000	0.0000	0.0043	0.0043	0.0000	0.0043	0.0000	0.0043	0.0038
P	0.0257	0.0239	0.0237	0.0273	0.0260	0.0242	0.0262	0.0242	0.0269	0.0621
Si	0.0095	0.0059	0.0053	0.0128	0.0021	0.0074	0.0015	0.0168	0.0005	0.0001

temperatures (as shown in Fig. 2). As thermal conductivity is also affected by the density of dislocations, grain boundaries, and the amounts of defects (i.e., porosity, cracks), more detailed microstructure tests, including atomic-level defect observations using transmission electron microscopy (TEM), positron lifetime annihilation spectroscopy (PALS), and micro-scale defect observations, i.e., X-ray computed tomography, and scanning electron microscopy (SEM), need to be performed, which remain as the future research work.

4.3. Thermal Expansion

The results for thermal expansion, average CTE, and instantaneous CTE all show excellent agreement between samples with very small variations in the values as exemplified by the small standard error of estimate. Based upon these results, the thermal expansion properties of AM GRCop-42 and GRCop-84 have excellent reproducibility regardless of starting powder, parameters, or machine.

Prior measurements were conducted for extruded GRCop-42 and GRCop-84 for the Reusable Launch Vehicle Second Generation program at NASA [30]. These samples from two GRCop-42 and five GRCop-84 powder lots also showed excellent reproducibility with similar standard errors of estimate as their AM counterparts. The extruded and AM thermal expansion curves are compared in Fig. 12. No 95% confidence interval is plotted because it again fell within the width of the line.

Examination of the regression lines indicated that there is a

difference in behavior. For GRCop-84, there is no overlap in the thermal expansion curves except at 20 $^{\circ}$ C. Otherwise, the AM GRCop-84 samples show a consistently lower thermal expansion than the extruded samples.

The amount of Cr_2Nb was generally lower for the AM samples than the extruded samples based upon the extraction data and calculated weight fraction of the extruded GRCop-84 samples. Given that the thermal expansion generally decreases with increasing Cr_2Nb , this is an unexpected result. Strong crystallographic texture is likely in these samples and may play a role in this result. Additional work is ongoing using electron backscattered diffraction (EBSD) to quantify the degree and orientation of any texture.

The results for AM GRCop-42 are more complex as the thermal expansion is less than the extruded GRCop-42 up to $\sim\!750\text{--}800\,^{\circ}\text{C}$ and then becomes slightly greater above $\sim\!850\text{--}900\,^{\circ}\text{C}$. The initially lower thermal expansion may be partially explained by the slightly higher than nominal Cr₂Nb content of some AM GRCop-42 samples. This is not a total explanation as Samples GRCop-42–4, GRCop-42–1, GRCop-42–5, and GRCop-42–6 have lower Cr₂Nb contents with Samples GRCop-42–1, GRCop-42–5, and GRCop-42–6 being notable because of their low Cr₂Nb and high Cr precipitate weight fractions. Texture may also play a role in this phenomenon.

The total weight fractions of Cr_2Nb and Cr precipitates in the AM GRCop-42 samples were greater than the nominal amount of Cr_2Nb in the extruded GRCop-42 samples. Samples GRCop-42–4 and GRCop-42–6 had slightly lower total Cr_2Nb and Cr precipitates. The Cr_2Nb and Cr may combine to reduce the thermal expansion at lower temperatures.

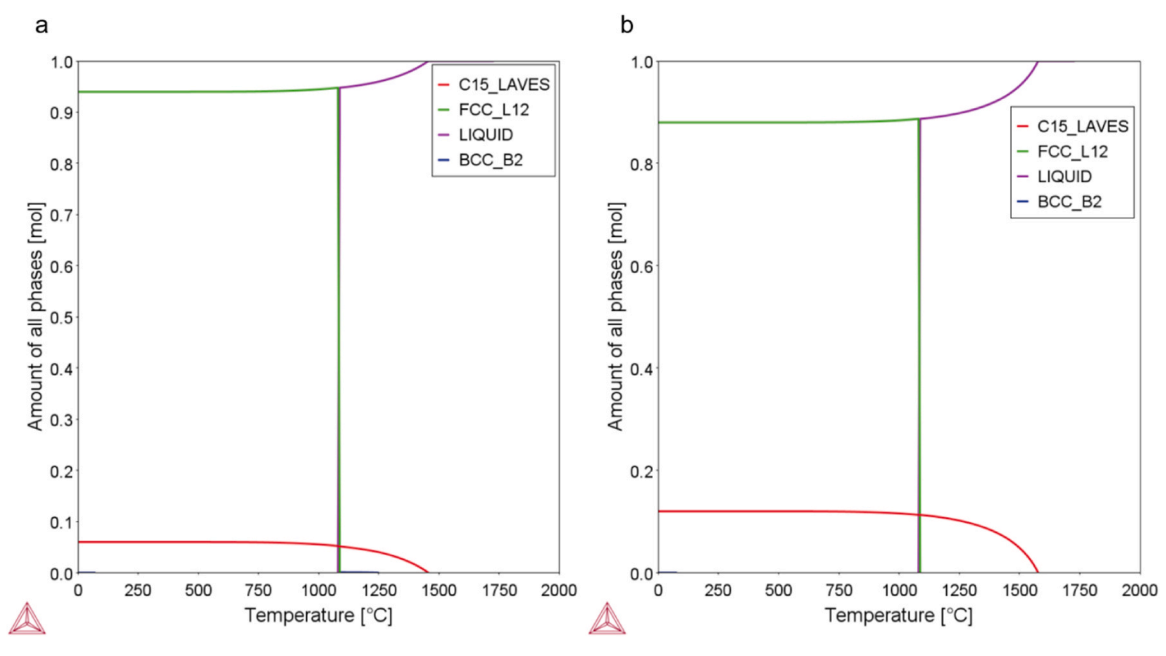


Fig. 12. Phases at different temperatures (a): GRCop-42. (b): GRCop-84.

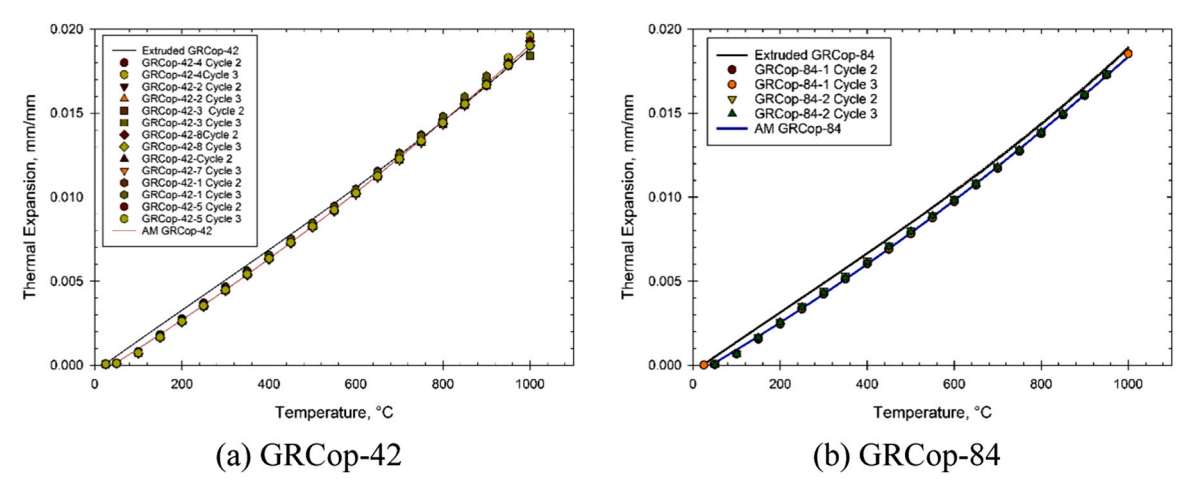


Fig. 13. Extruded and AM Thermal Expansion Comparisons.

However, as the temperature increases, the solubility of Cr in the copper matrix increases, and the amount of Cr precipitates decreases. Based upon standard Cu-1 Cr alloy heat treatments [30], all Cr should be dissolved into the Cu matrix somewhere between 900 $^{\circ}\text{C}$ and 1000 $^{\circ}\text{C}$. The loss of Cr precipitates should increase the average and instantaneous CTEs relative to the extruded GRCop-42 and creates a crossover in the thermal expansion. The dissolving of the Cr appears to be the likely reason for the crossover.

Regardless of the small differences, both AM GRCop-42 and GRCop-84 are similar to past wrought measurements and extremely consistent with regards to each other. This strongly indicates that the thermal expansion variability from differing AM processing parameters, machines, and parameters will be minimal in a production environment.

5. Conclusions

Thermal conductivities and thermal expansion coefficients (CTE) for eight GRCop-42 samples and two GRCop-84 samples were measured from room temperature to 700 °C for thermal conductivity and 1000 °C for thermal expansion. These GRCop alloy samples were made with powders from different feedstock lots and with various L-PBF machines at several vendors. Equations were developed over the temperature range of 25–700 °C to predict thermal conductivity and 20–1000 °C for CTE (average and instantaneous). Several observations and conclusions can be drawn from these experimental results.

- The results demonstrated that thermophysical properties of GRCop-42 and GRCop-84 alloys produced with L-PBF demonstrate highly repeatable results independent of processing parameters, powder feedstock differences, and machine type. This implies consistency within parts and between parts and provides designers higher confidence in meeting design minimum values during the manufacturing process, which means increased reliability and risk reduction.
- \bullet The thermal conductivities of the GRCop-42 samples exhibited a variation of \pm 4%, which marginally surpasses the inherent instrument variability of \pm 3%. This additional variation between samples, exceeding the known instrument variability, could potentially be associated with the amounts of solute atoms dissolved in the Cu matrix. While no explicit correlation was identified, it was demonstrated that these elements could be significant factors. Further research, employing comprehensive atomic-scale and micro-scale studies, is required in the future to fully elucidate the variations in thermal conductivity.
- For the AM GRCop-42 and GRCop-84 thermal expansion samples, the AM L-PBF thermal expansion behavior was statistically significantly different from the extruded material but was consistent for each

alloy. The mostly lower thermal expansion would result in lower thermally induced stresses, less permanent deformation from thermally induced strains, and longer LCF lives.

It is important to recognize that while L-PBF parts can be successfully built in a controlled laboratory setting, the translation to a production environment is not always seamless. The presence of variations across many machines and powder lots necessitates a comprehensive understanding of the variability of properties across multiple vendors operating independent of each other. The repeatability and reproducibility throughout the commercial supply chain holds paramount significance for designers aiming to ensure that parts align with expected properties and operational requirements. Specifically, the thermal conductivity and thermal expansion emerge as crucial in the design process. By leveraging the knowledge of variations in thermal properties, it becomes possible to establish process capabilities and design guidelines that facilitate ongoing commercial utilization and further research endeavors.

CRediT authorship contribution statement

Yehong Chen: Methodology, Validation, Formal analysis, Investigation, Data curation, Writing – original draft. Congyuan Zeng: Methodology, Validation, Formal analysis, Investigation, Writing – original draft. Huan Ding: Validation, Formal analysis, Investigation. Selami Emanet: Validation, Formal analysis, Investigation. Paul R. Gradl: Conceptualization, Resources, Writing – review & editing, Funding acquisition. David L. Ellis: Investigation, Resources, Writing – review & editing. Shengmin Guo: Conceptualization, Supervision, Writing – review & editing, Project administration, Funding acquisition.

Declaration of Competing Interest

The authors declare that they have no known competing financial interests or personal relationships that could have appeared to influence the work reported in this paper.

Data Availability

The data that has been used is confidential.

Acknowledgement

This work is partially supported by NSF #OIA-2118756 and NASA EPSCOR. The use of instruments housed within the LSU Shared Instrumentation Facilities (SIF), a part of LAMDA (Grant Number NSF #OIA-

1946231) Core User Facilities, is acknowledged. The authors would also like to thank Dereck Johnson at NASA Glenn Research Center for conducting all thermal expansion measurements.

Appendix A. Supporting information

Supplementary data associated with this article can be found in the online version at doi:10.1016/j.mtcomm.2023.106665.

References

- [1] K.R. Rupesh, A.M. Priya, B. Sundarakrishnan, R. Venkatesan, B.S. Lakshmi, S. Jayachandran, 2,2'-bipyridyl based copper complexes down regulate expression of pro-inflammatory cytokines and suppress MAPKs in mitogen induced Peripheral blood mononuclear cells, Eur. J. Med Chem. 45 (2010) 2141–2146.
- [2] A.R. Kini, D. Maischner, A. Weisheit, D. Ponge, B. Gault, E.A. Jägle, D. Raabe, Insitu synthesis via laser metal deposition of a lean Cu-3.4Cr-0.6Nb (at%) conductive alloy hardened by Cr nano-scale precipitates and by Laves phase microparticles, Acta Mater. 197 (2020) 330-340.
- [3] D. Raabe, D. Mattissen, Microstructure and mechanical properties of a cast and wire-drawn ternary Cu-Ag-Nb in situ composite, Acta Mater. 46 (1998) 5973–5984.
- [4] D. Raabe, S. Ohsaki, K. Hono, Mechanical alloying and amorphization in Cu–Nb–Ag in situ composite wires studied by transmission electron microscopy and atom probe tomography, Acta Mater. 57 (2009) 5254–5263.
- [5] H. You, S. Yang, B. Ding, H. Yang, Synthesis of colloidal metal and metal alloy nanoparticles for electrochemical energy applications, Chem. Soc. Rev. 42 (2013) 2880–2904.
- [6] K.-H. Huynh, X.-H. Pham, J. Kim, S.H. Lee, H. Chang, W.-Y. Rho, B.-H. Jun, Synthesis, properties, and biological applications of metallic alloy nanoparticles, Int. J. Mol. Sci. 21 (2020) 5174.
- [7] P. Berge, S. Kim, E. Gibson, J. Verhoeven, An air melting technique for preparing Cu-Cr alloys, JOM 50 (1998) 42–43.
- [8] M. Morris, D. Morris, Microstructures and mechanical properties of rapidly solidified Cu Cr alloys, Acta Metall. 35 (1987) 2511–2522.
- [9] W. He, E. Wang, L. Hu, Y. Yu, H. Sun, Effect of extrusion on microstructure and properties of a submicron crystalline Cu–5 wt% Cr alloy, J. Mater. Process. Technol. 208 (2008) 205–210.
- [10] D. Ellis, G. Michal, Precipitation strengthened high strength, high conductivity Cu-Cr-Nb alloys produced by chill block melt spinning. Final report Ph. D. Thesis, Case Western Reserve Univ., Cleveland, OH (USA), 1989.
- [11] S. Jia, M. Zheng, P. Liu, F. Ren, B. Tian, G. Zhou, H. Lou, Aging properties studies in a Cu-Ag-Cr alloy, Mater. Sci. Eng.: A 419 (2006) 8-11.
- [12] J. Correia, H. Davies, C. Sellars, Strengthening in rapidly solidified age hardened Cu Cr and Cu Cr Zr alloys, Acta Mater. 45 (1997) 177–190.
- [13] D. Stork, P. Agostini, J.-L. Boutard, D. Buckthorpe, E. Diegele, S. Dudarev, C. English, G. Federici, M. Gilbert, S. Gonzalez, Developing structural, high-heat flux and plasma facing materials for a near-term DEMO fusion power plant: the EU assessment, J. Nucl. Mater. 455 (2014) 277–291.
- [14] S. Zinkle, S. Fabritsiev, Copper alloys for high heat flux structure applications, atomic and plasma-material interaction data for fusion (supplement to Nuclear Fusion) 5 (1994) 163.
- [15] H.C. de Groh, D.L. Ellis, W.S. Loewenthal, Comparison of GRCop-84 to other Cu alloys with high thermal conductivities, J. Mater. Eng. Perform. 17 (2008) 594–606.
- [16] S. Fabritsiev, S. Zinkle, B. Singh, Evaluation of copper alloys for fusion reactor divertor and first wall components, J. Nucl. Mater. 233 (1996) 127–137.
- [17] X. Guo, Z. Xiao, W. Qiu, Z. Li, Z. Zhao, X. Wang, Y. Jiang, Microstructure and properties of Cu-Cr-Nb alloy with high strength, high electrical conductivity and good softening resistance performance at elevated temperature, Mater. Sci. Eng.: A 749 (2019) 281–290.
- [18] M. Ma, Z. Li, Z. Xiao, H. Zhu, X. Zhang, F. Zhao, Microstructure and properties of a novel Cu-Cr-Yb alloy with high strength, high electrical conductivity and good softening resistance, Mater. Sci. Eng.: A 795 (2020), 140001.
- [19] K.R. Anderson, J.R. Groza, Microstructural size effects in high-strength highconductivity Cu-Cr-Nb alloys, Metallurgical and Materials Transactions 32 (2001) 1211.
- [20] K.R. Anderson, J.R. Groza, R.L. Dreshfield, D. Ellis, High-performance dispersionstrengthened Cu-8 Cr-4 Nb alloy, Metall. Mater. Trans. A 26 (1995) 2197–2206.

- [21] K. Cooper, J. Lydon, M. LeCorre, Z. Jones, D. Scannapieco, D. Ellis, B. Lerch, Three-dimensional printing GRCop-42, NASA/TM (2018), 220129.
- [22] D.L. Ellis, GRCop-84: A high-temperature copper alloy for high-heat-flux applications, (2005).
- [23] D.L. Ellis, B.A. Lerch, Improvement of GRCop-84 through the addition of zirconium, 2012.
- [24] R.P. Minneci, E.A. Lass, J.R. Bunn, H. Choo, C.J. Rawn, Copper-based alloys for structural high-heat-flux applications: a review of development, properties, and performance of Cu-rich Cu-Cr-Nb alloys, Int. Mater. Rev. 66 (2021) 394–425.
- [25] S. Landes, T. Suresh, A. Prasad, T. Letcher, P. Gradl, D. Ellis, Investigation of additive manufactured GRCop-42 alloy developed by directed energy deposition methods. ASME International Mechanical Engineering Congress and Exposition, American Society of Mechanical Engineers, 2020. V004T004A026.
- [26] P.R. Gradl, C.S. Protz, D.L. Ellis, S.E. Greene, Progress in additively manufactured copper-alloy GRCop-84, GRCop-42, and bimetallic combustion chambers for liquid rocket engines, International Astronautical Congress (IAC), 2019.
- [27] P.R. Gradl, C. Protz, J. Fikes, D. Ellis, L. Evans, A. Clark, S. Miller, T. Hudson, Lightweight thrust chamber assemblies using multi-alloy additive manufacturing and composite overwrap, AIAA Propulsion and Energy 2020, Forum (2020) 3787.
- [28] S.M. Arnold, J. Butler, Daniel T., M.-J. Pindera, Analysis of Factors Affecting the Performance of RLV Thrust Cell Liners, NASA Glenn Research Center, Cleveland, OH. 2004.
- [29] R. Citarella, M. Ferraiuolo, V. Giannella, Thermostructural numerical analysis of the thrust chamber of a liquid propellant rocket engine, Materials 15 (2022) 5247.
- [30] D.L. Ellis, D.J. Keller, M. Nathal, Thermophys. Prop. GRCop 84 (2000).
- [31] N. Dubrovinskaia, L. Dubrovinsky, S. Saxena, B. Sundman, Thermal expansion of chromium (Cr) to melting temperature, Calphad 21 (1997) 497–508.
- [32] D.L. Ellis, G.M. Michal, N.W. Orth, Production and processing of Cu-Cr-Nb alloys, 1990.
- [33] D.L. Ellis, G.M. Michal, Precipitation strengthened high strength, high conductivity Cu-Cr-Nb alloys produced by chill block melt spinning, NASA Lewis Research Center, Cleveland, OH, 1989.
- [34] P.R. Gradl, C.S. Protz, Technology advancements for channel wall nozzle manufacturing in liquid rocket engines, Acta Astronaut. 174 (2020) 148–158.
- [35] S.T. Phillips, Advanced Manufacturing Branch Brochure, (2020).
- [36] P. Gradl, D.C. Tinker, A. Park, O.R. Mireles, M. Garcia, R. Wilkerson, C. Mckinney, Robust metal additive manufacturing process selection and development for aerospace components, J. Mater. Eng. Perform. 31 (2022) 6013–6044.
- [37] B. Zheng, Y. Zhou, J. Smugeresky, J. Schoenung, E. Lavernia, Thermal behavior and microstructural evolution during laser deposition with laser-engineered net shaping: part I. Numerical calculations, Metall. Mater. Trans. A 39 (2008) 2228–2236.
- [38] P.R. Gradl, D.C. Tinker, J. Ivester, S.W. Skinner, T. Teasley, J.L. Bili, Geometric feature reproducibility for laser powder bed fusion (L-PBF) additive manufacturing with Inconel 718, Addit. Manuf. 47 (2021), 102305.
- [39] J. Jhabvala, E. Boillat, T. Antignac, R. Glardon, On the effect of scanning strategies in the selective laser melting process, Virtual Phys. Prototyp. 5 (2010) 99–109.
- [40] P.R. Gradl, C.S. Protz, K. Cooper, D. Ellis, L.J. Evans, C. Garcia, GRCop-42 development and hot-fire testing using additive manufacturing powder bed fusion for channel-cooled combustion chambers, AIAA Propulsion and Energy 2019, Forum (2019) 4228
- [41] Netzsch-Proteus ver. 7.1 software manual.
- [42] P.R. Gradl, O.R. Mireles, C.S. Protz, C.P. Garcia, Metal Additive Manufacturing for Propulsion Applications, American Institute of Aeronautics and Astronautics, Inc., 2022
- [43] C. Zeng, B. Zhang, A.H. Ettefagh, H. Wen, H. Yao, W. Meng, S. Guo, Mechanical, thermal, and corrosion properties of Cu-10Sn alloy prepared by laser-powder-bedfusion additive manufacturing, Addit. Manuf. 35 (2020), 101411.
- [44] L.U. Thomas-Ogbuji, D.L. Humphrey, L. Greenbauer-Seng, Oxidation behavior of GRCop-84 (Cu-8Cr-4Nb) at intermediate and high temperatures, NASA/CR (2000), 210369
- [45] NIST Chemistry WebBook, SRD 69.
- [46] D.L. Ellis, G.M. Michal, N.W. Orth, Production and processing of Cu-Cr-Nb alloys, Scr. Metall. Et. Mater. 24 (1990) 885–890.
- [47] D. Ellis, A. Misra, R. Dreshfield, Effect of hydrogen exposure on a Cu-8 Cr-4 Nb alloy, NASA Lewis Research Center, Cleveland, OH, 1993.
- [48] F. Pawlak, K. Reichel, The effect of impurities on the electrical conductivity of copper, Zeit Metallkd. 47 (1956) 347.
- [49] R. Franz, G. Wiedemann, Ueber die Wärme-Leitungsfähigkeit der Metalle, Ann. der Phys. 165 (1853) 497–531.
- [50] J. Jeon, D. Bae, Effect of cooling rate on the thermal and electrical conductivities of an A356 sand cast alloy, J. Alloy. Compd. 808 (2019), 151756.
- [51] J.R. Davis, Copper and copper alloys, ASM international, 2001.